Superior high-temperature properties and deformation-induced planar faults in a novel L12-strengthened high-entropy alloy

Y.L. Zhaoa,d, T. Yanga, Y.R. Lia, L. Fanb, B. Hana,d, Z.B. Jiaob, D. Chena,
C.T. Liua,c, J.J. Kaia,d,*

ᵃ Department of Mechanical Engineering, City University of Hong Kong, Hong Kong, China
ᵇ Department of Mechanical Engineering, The Hong Kong Polytechnic University, Hong Kong,
China
ᶜ Department of Materials Science and Engineering, City University of Hong Kong, Hong Kong,
China
ᵈ Center for Advanced Nuclear Safety and Sustainable Development, City University of Hong
Kong, Hong Kong, China

ABSTRACT

We developed a novel high-performance L1$_2$-strengthened high-entropy alloy (HEA) in the multicomponent Ni- Co-Fe-Cr-Al-Nb system. The phase transformation, mechanical properties and associated deformation behaviors were systematically investigated through combinational analyses involving the three-dimensional atom probe tomography (3D-APT), transmission electron microscopy (TEM) and first-principles calculations. In contrast to conventional alloys that generally strengthened by Ni3(Al, Ti)-type precipitates, a high density of coherent L12 nanoprecipitates with a new chemical constitution of (Ni, Co, Fe, Cr)$_3$(Al, Nb) can be controllably introduced via elaboratively tuning the content of Al and Nb, resulting in a large lattice misfit of ~0.78% that rarely achieved in previous HEAs. The newly developed (Ni$_2$Co$_2$FeCr)$_{92}$Al$_4$Nb$_4$ HEA enables excellent tensile properties at a large temperature window from room temperature to 870 °C. More remarkably, an anomalous growth in yield strength can be observed at the temperatures above 600 °C, showing a peak yield

stress over 720 MPa when deformed at 760 °C, which surpasses most of the previous L1$_2$-strengthened HEAs, as well as the commercial superalloys. Detailed TEM analyses revealed that the multicomponent L1$_2$ precipitates are mainly sheared by the super-partial dislocations, forming superlattice intrinsic stacking fault (SISF) loops coupled with antiphase boundaries (APBs). Such an interesting deformation substructure enables sustained work hardening and produces high tensile strengths at the high temperatures. The underlying mechanisms of those SISF loops were carefully discussed, which could be possibly ascribed to the local elemental segregation on the planner faults.

Keywords: High-entropy alloys; High-temperature strength; Deformation mechanisms; Planar faults

1. Introduction

Metallic alloys strengthened by dispersed nanoparticles provide the basis of designing multifarious load-bearing materials for engineering applications. The recent discovery of L1$_2$-strengthened multicomponent high-entropy alloys (HEAs) [1-3] has been demonstrated as a new paradigm for developing advanced structural materials with superior mechanical performance due to their unique microstructures and intriguing work-hardening behaviors [4-8]. In particular, owing to the similar microstructure ($\gamma + \gamma'$) to the commercial Ni-based superalloys, these L1$_2$-strengthened HEAs are considered as promising alternatives for heat-resistant materials. While extensive studies have been carried out during recent years, there are two primary limitations on their widespread applications. First, most of the L1$_2$-strengthened HEAs studied were mainly confined to the Al-Ti-bearing systems, relying on introducing the L1$_2$ Ni$_3$(Al, Ti)-type particles for hardening purpose. These HEAs systems were generally reported with low solvus temperatures and associated insufficient volume

fractions of the L1$_2$ precipitates, leading to quite limited temperature capacities of these alloys. For example, He et al. [5] reported that only a small volume fraction of coherent L12 nanoparticles (~20%) can be formed in the (FeCoNiCr)$_{94}$- Ti$_2$Al$_4$ alloy. Moreover, it is worth mentioning that these Ni3(Al, Ti)-type nanoparticles could only be thermally stabilized in a relatively low temperature range (650~850 °C), making them unsatisfactory for many practical applications. Similar results have also been reported in the Al$_{0.5}$CuCrFeCoNi HEA system [9], where the L1$_2$-solvus temperature lies between 800 °C and 850 °C. In addition, the precipitate/matrix lattice misfits are usually small in these Al-Ti-bearing HEAs [6,10], resulting in a limited coherency strengthening due to the less pronounced elastic interaction between the dislocations and precipitates [11]. Thus, to address these critical issues for achieving enhanced high-temperature performance, compositional optimization is urgently needed.

On the other hand, the high-temperature deformation behaviors and mechanisms of the L1$_2$-strengthened HEAs are far from being explored, which greatly hinders the further development of such materials. Previous studies indicated that benefiting from the combined merits of both the ductile multicomponent matrix and precipitates, the L1$_2$-strengthened HEAs enable a great capacity to get a superior strength-ductility combination in a wide temperature window. Indeed, various toughing mechanisms, such as deformation-induced nano-twinning [12], dislocation- induced microbands [4] and dynamic refined SFs [7], can be readily activated in the L1$_2$-strengthened HEAs deformed at cryogenic and room temperatures. However, whether those toughening mechanisms can be effectively operated at the elevated temperatures is still an open question. It was, in fact, suggested by several investigators that the toughing mechanisms triggered at room temperature are generally inapplicable during the high-temperature deformation due to the growing thermal effect. For example, in Ni-based

superalloys [13], plastic deformation at room temperature is typically dominated by the glide of $1/2<110>$ super-dislocations at $\{111\}$ planes. With increasing temperature, dislocation cross-slip on the cubic $\{100\}$ planes starts to operate, resulting in quite different dislocation substructures associated with the variations of flow stresses. Therefore, to develop superior heat-resistant $L1_2$-strengthened HEAs, it is imperative to get a deep insight into the underlying dislocation behaviors and the dislocation-precipitates interactions at high temperatures, which are, however, remains poorly understood until now.

To overcome these challenges, here we designed a novel dual-phase HEA reinforced by the unique $(Ni, Co, Fe, Cr)_3(Al, Nb)$-type multicomponent $L1_2$ nanoparticles, generating superior mechanical properties at both ambient and elevated temperatures. First of all, to achieve the enlarged precipitate/matrix lattice misfit and increased solvus temperature of $L1_2$ precipitates, the Nb element was chosen here due to its intrinsic larger atomic size and higher melting temperature than that of the Ti element. By this way, we successfully achieved a higher volume fraction of the $L1_2$ precipitates and associated more pronounced strengthening efficiency at elevated temperatures. Secondly, by means of multiscale analyses of APT, TEM and first-principles calculations, basic mechanisms of alloying effects on the phase stabilities of the compositionally complex precipitates were clearly elucidated. More importantly, we systematically investigated the temperature dependence of tensile strength of the newly developed $L1_2$-strengthened HEA, and the detailed deformation micro-mechanisms were also carefully discussed. The results achieved here are both technically and scientifically important to the accelerated development of high-performance HEAs for elevated temperature applications.

2.Materials and methods

2.1Alloys preparation

Our previous study indicated that deviating from the equal-molar restriction by decreasing the Fe and Cr concentrations in the NiCo- FeCr quaternary system will greatly widen the $L1_2$ phase region and improves the alloy design space [12]. In light of this, the Ni2Co2FeCr was selected as the base alloy in our present study, whereas the Al and Nb elements were controllably added to introduce precipitation hardening. For convenience, the alloys studied here will be labeled by their Al and Nb concentrations, referred as the Al4, Nb4, Al2Nb4, and Al4Nb4 HEA, respectively. A small amount of boron (0.02 wt.%) will be added to all the designed HEAs based on the conventional wisdom in the superalloys for grain-boundary strengthening [14,15]. All ingots were repeatedly melted in high-purity Ar atmosphere and cast into slats with a dimension of 70 mm (length)×12 mm (width)×5 mm (thickness). After that, a homogenization heat treatment was conducted at 1200 °C for 2 h to assuage elemental segregation during solidification, followed by cold rolling into thin sheets with a total thickness reduction of ~66%. The cold-rolled sheets were subsequently recrystallized at 1200 °C for 1.5 min, followed by oil quenching and finally aged at 800 °C with different durations.

2.2Microstructural characterizations and mechanical tests

The as-prepared alloys were systematically characterized including the microstructures, mechanical properties, and deformation micro-mechanisms. Phase identification was performed by an X-ray diffraction (XRD, Rigaku Smart Lab) equipped with a monochromator. The crystallographic information was collected in the range of 2θ= 20°~100° with a scanning speed of 2°/min. Lattice misfit was determined

by deconvolution of the (220) diffraction peak, following the equation of $\delta=2(\alpha_{particle}-\alpha_{matrix})/(\alpha_{particle}+\alpha_{matrix})$, in which the a refers to the lattice parameter of each phase [16]. Scanning electron microscopy (SEM) and transmission electron microscopy (TEM) with selected area diffraction patterns (SADPs) were also conducted for further confirmations.

Microhardness was measured using a Vickers microhardness tester using a load of 2 N. Dog-bone-shaped specimens with a gauge length of 12.5 mm and a cross-section dimension of 3.2×1.5 mm^2 were fabricated by an electro-discharge machining (Sodick, AQ360LX) for uniaxial tensile tests, which were performed on a Material Testing System (MTS) machine with a constant strain rate of 1×10^{-3} s^{-1}. At least two specimens were measured for each condition to ensure data reliability. To eliminate temperature fluctuation on the gauge-length section, before testing the tensile specimens were stayed in an electric furnace for an additional 10 min once the setting temperature was reached. The microscopic deformation mechanisms for the tensile specimens were further explored using a JEM-2100F TEM operated at 200 kV. TEM specimens from the uniform-elongated sections were manually ground down to ~50 mm, punched into F3 mm disks and subsequently thinned by an ion-milling method.

2.3 Theoretical calculations

Density functional theory (DFT) [17] calculations were performed using the Vienna Ab initio Simulation Package (VASP) [18]. The projector augmented wave (PAW) method [19] was used to describe the interactions between core electrons and valence electrons. The exchange-correlation functional was schemed by the generalized gradient approximation (GGA) described by the Perdew-Burke-Ernzerhof (PBE) parametrization [20]. The chemical disorder was considered by using the Special Quasi-

random Structure (SQS) as embedded in the Alloy Theoretic Automatic Toolkit (ATAT) [21]. In particular, structures of L12, D019 and D022 phases were studied. The electronic Bloch wave functions were expanded in a plane-wave basis set with an energy cutoff of 350 eV and sampled by G-centered 3×3×3, 3×3×3 and 5×5×3 Monkhorst-Pack k-meshes [22] for the $L1_2$, D019, and $D0_{22}$ phases, respectively. All calculations were performed with spin polarization allowing the full relaxation of magnetic moments. For the $L1_2$ and D019 phases, the equilibrium lattice parameters were first determined by fitting the energy-volume curves to the third-order Birch-Murnaghan equation of states (EOS) [23]. Then the internal atomic positions were fully relaxed with the convergence criteria of 10^{-5} eV for total energy and 0.005 eV/Å for Hellmann-Feynman force, respectively. For the $D0_{22}$ phase, the geometry optimization was directly performed with the same convergence criteria. The chemical stability was estimated by the enthalpy of formation at 0 K ($\Delta_f H^0$) and calculated by the following equation [24]:

$$\Delta_f H^0 = E_{sp} - \sum_i n_i \mu_i \qquad \Box 1 \Box$$

Here E_{sp} is the total energy of supercell, n_i and μ_i are the number and chemical potential for atoms of the i_{th} kind in the supercell, respectively. The chemical potential for each kind of atom was approximated by the total energy of their bulk counterpart with the most stable phase (face-centered cubic structure, FCC, for Ni and Al, hexagonal close-packed structure for Co, and body-centered cubic structure for Nb).

3.Results

3.1Mechanical properties at ambient temperature

To start with, microhardness measurements were carried out to determine the

optimum aging condition for precipitation hardening of the (Al, Nb)-bearing HEAs. Fig. 1(a) shows the evolution of microhardness as a function of aging time. The Al2Nb4 and Al4Nb4 HEAs exhibit similar hardening behaviors, where the microhardness peaks at 24 h, and steadily decreases with increasing aging time to 168 h. The microhardness of Nb4 HEA displays a monotonic increment with two growth rates separated by the point of 24h's aging. This peculiar behavior certainly deviates from the hardening behavior of the Al2Nb4 and Al4Nb4 HEAs, which is presumably due to the occurrence of additional precipitation process and worthy of our investigation in a future report. For the Al4 HEA, negligible variation in microhardness values was found as the aging time prolonged (not shown here), suggesting that there are no precipitates formed at the current aging conditions. In contrast, it is evident that the Al4Nb4 alloy aged at 800 °C for 24 h shows the highest microhardness (~440 HV), suggesting a remarkable precipitation hardening effect.

Based on the above observations, the alloys aged at 800 °C for 24 h were subsequently chosen for tensile tests at room temperature. The representative engineering stress-strain curves are shown in Fig. 1 (b). It is evident that the Al4Nb4 alloy exhibits the highest tensile strength, with an ultimate tensile strength (UTS) of ~1232 MPa and yield stress (YS) of ~ 850 MPa, but almost without ductility loss as compared to the Al2Nb4 and Nb4 HEAs, i.e. ~30% in elongation. The precipitate-free Al4 HEA is the weakest among all the HEAs primarily due to the absence of strong barriers for dislocation motions.

3.2 Microstructures and phase identifications

Fig. 2 represents the microstructures of the Al4, Nb4, Al2Nb4 and Al4Nb4 HEAs aged at 800 °C for 24 h, depicting the precipitate morphologies and distributions at the

grain-boundary triple junctions. Noted that no discernible precipitates can be detected in the Al4 HEA, which is consistent with the aforementioned mechanical tests. In contrast, two categories of precipitates with different morphologies can be observed in the Nb-bearing HEAs. The addition of Al element appears to play an important role in the precipitation reactions of the Nb-bearing HEAs. As the Al content increases from 0 to 4 at.% (Fig. 2 (b-d)), despite a small volume of precipitates (50-500 nm in size) lying along the grain boundary, the dominated microstructures in the grain interior gradually change from needle-shaped (the Nb4 alloy) to needle-cuboidal mixed (the Al2Nb4 alloy) and to fully cuboidal precipitates (the Al4Nb4 alloy).

The X-ray diffraction (XRD) results were presented in Fig. 3. Besides the main peaks of FCC structure, the small peaks corresponding to L12 and D019 structures can be clearly detected (Fig. 3) in the Nb4, Al2Nb4 and Al4Nb4 HEAs. Those $D0_{19}$ peaks somewhat become weak with the increase of Al contents, indicating the volume fraction of $D0_{19}$ phase decreases accordingly. Based on the SEM and XRD investigations, the needle-shaped precipitates were identified as the $D0_{19}$ phase while the cuboidal precipitates were identified as the $L1_2$ phase, the morphologies of which are consistent with those reported in conventional superalloys. For the Al4Nb4 HEA with the $L1_2$/FCC microstructures, the lattice misfit can be derived from the deconvolution of the (220) diffraction peak (Fig. 3(b)). Noted that the deconvolution was performed by only considering the contributions from the $L1_2$ and FCC phases since no $D0_{19}$ peaks were detected within 72°-77° The result shows that the lattice constant of the L12 precipitates (0.3615 nm) exceeds that of the FCC matrix (0.3587 nm) and gives rise to a positive lattice misfit (~0.78%), which is contrary to the negative misfit that is commonly found in Ni-based superalloys. Such a positive lattice misfit was suggested to contribute to a better hightemperature creep resistance [25].

The phase structures were further confirmed by TEM analyses. Fig. 4(a) shows a typical bight-field TEM image of the precipitates in the Nb4 HEA, concomitant with efforts of selected-area diffraction patterns (SADPs), Energy Dispersive X-ray spectroscopy (EDS) and high-resolution TEM (HRTEM) image in Fig. 4 (b-d). The SADPs collected from the zone axis paralleled to $[110]_m$ and $[112]_m$ (matrix) demonstrated the FCC crystal structure of the matrix and the $D0_{19}$ structure of the needle-shaped precipitates in the Nb4 HEA. Furthermore, compositional analysis using the EDS indicates that the Ni and Nb elements have a strong tendency to partitioning into the D019 precipitates, whereas the Cr and Fe elements are more likely to stay inside the FCC matrix. The Co element stands rather neutral with a slight preference to the FCC matrix.

Similarly, Fig. 5 shows the bright-field TEM image of the cuboidal precipitates in the Al4Nb4 HEA. The inset of Fig. 5 (a) presents the diffraction pattern acquired from the [001] zone axis, demonstrating the ordered $L1_2$ structure of the precipitates, as well as the coherent relationship between the L12 precipitates and FCC matrix. This can be

further verified by the dark-field TEM micrograph taken from the superlattice spot corresponding to the $L1_2$ reflections in Fig. 5(b), in which illuminated cuboidal precipitates are uniformly distributed throughout the FCC matrix. Furthermore, the elemental distribution of individual element was quantitively determined by APT, as shown in Fig. 5(c). The proximity histogram for the elemental partitioning behavior across the precipitates/matrix interface was presented in Fig. 6. It clearly reveals that the Ni, Nb and Al elements primarily partition into the $L1_2$ precipitates, leading to a multicomponent $(Ni, Co, Fe, Cr)_3(Al, Nb)$-type ordered nanoparticles.

In addition, the crystal structures of the precipitates in the Al2Nb4 HEA were also

carefully investigated, where the needle-shaped and the cuboidal precipitates were determined to be the $D0_{19}$ and $L1_2$ phase, respectively. Phases precipitated along the grain boundaries in the Nb4, Al2Nb4 and Al4Nb4 HEA were identified as the $D0_{19}$ phase. The volume fractions of the dominated precipitates were further estimated by the projected areal fraction and statistically obtained from the SEM and TEM images via ImageJ software. Specifically, the volume fractions of $D0_{19}$ precipitate in the Nb4 and Al2Nb4 HEA were estimated to be around 32.1%, 11.6%, respectively. The sizes of $D0_{19}$ precipitates in these two alloys are very similar with a width of about 34.5±14.1 nm. Compared to the $L1_2$ precipitates in the Al2Nb4 HEA (volume fraction of 22.0% and mean size of 15.1±4.2 nm), the population of the $L1_2$ precipitates in the Al4Nb4 HEA appears much higher (volume fraction of ~51%, also higher than the Al-Ti-bearing HEAs) with a larger mean size of 39.0 § 9.7 nm. Noted that the precipitate size was obtained from an area-equivalent diameter ($size = 2\sqrt{area/\pi}$).) The values of the area fractions are relative to the solid solution matrix, ignoring the contributions of the large phases at the grain boundaries.

3.3 Temperature-dependent mechanical properties

High-temperature mechanical properties of the Al4Nb4 HEA, which exhibits the best performance at ambient temperature, were carefully evaluated, as presented in Fig. 7(a). Both the UTS and YS obtained from the tensile engineering stress-strain curves were plotted as a function of temperature, alongside with the high-temperature mechanical properties of Waspaloy (Ni-based superalloy) [26], Co-Al-W-Ta-B (Co-based superalloy) [27] and other HEAs [28-31] (Fig. 7(b)). Excellent high-temperature performance can be achieved in the present Al4Nb4 HEA, especially at temperatures above 600 °C. The strength of the Al4Nb4 HEA is stronger than that of most previously

studied solid-solution-strengthened HEA, i.e. CoCrFeNiMn [31], the L12-strengthened HEAs (such as $(FeCoNiCr)_{94}Ti_2Al_4$ [30]) and the Co-based superalloy across the entire temperature range. At 600 °C, the YS and UTS of the Al4Nb4 alloy were measured to be ~681 MPa and ~991 MPa, respectively. More interestingly, the newly developed Al4Nb4 HEA exhibits YS anomalies at 760 °C with a YS of ~720 MPa and a UTS as high as ~900 MPa, which even exceeds that of the commercial Ni-based Waspaloy superalloy to some extent. More importantly, unlike the case of the Waspaloy where its flow stress precipitously drops to 275 MPa after yielding at 870 °C, a high strength of ~530 MPa can be still achieved in the Al4Nb4 alloy at the same temperature (Fig. 7(a)). Given the discrete distribution and the very small volume fraction (less than 1%), those D019 particles would play a very limited effect on both the strength and ductility of our present Al4Nb4 alloy. The pronounced precipitation hardening effect in the Al4Nb4 HEA thus could be primarily attributed to the relatively large lattice misfit (~0.78%) between the FCC matrix and the L12 precipitates, which is approximately threefold higher than that of the previous $(FeCoNiCr)_{94}Ti_2Al_4$ HEA (~0.26%) [10] and even larger than that of the $L1_2$-strengthened Co-Al-W alloy (~0.53%) [32], leading to a higher stress to overcome the strain field and prevent the shearing of the precipitates in the wake.

3.4 Deformation substructures

To get an in-depth understanding of the deformation behaviors and the associated strengthening mechanisms of the present Al4Nb4 HEA, dislocation substructures at different temperatures were carefully examined at a similar tensile strain of ~5%. Fig. 8 presents the typical structural features of the alloys deformed at room temperature. The deformation mode appears to be dominated by stacking faults (SFs), which would

be more discernible when imaged using relrods dark-field technique [33], as shown in Fig. 8(b). SFs spanning across the matrix and precipitates (Fig. 8 (c, d)) can be frequently observed near the incipient {111} slip trace. The natures of those SFs were further identified by the high-resolution TEM (HRTEM) analysis. The stacking sequence of the different SFs is presented in Fig. 8 (e, f), where both the intrinsic and extrinsic SFs can be clearly observed in either matrix or precipitate.

TEM images presented Fig. 9 were taken from the specimen subjected to deformation at 760 °C. Distinctly different from the room-temperature deformation, abundant isolated SF loops within the precipitates can be observed. The average loop size was statistically measured to be 36.3±10 nm, which is comparable to the size of L1$_2$ precipitate (39.0±9.7 nm), implying that the SFs appear to extend over almost the entire precipitates. The close-up view highlighting the shearing of the precipitates by the SFs is illustrated in Fig. 9 (b, c). Evidently, the SFs couple with a small segment of APB can be cleared observed. To determine the nature of the SF loop, Burgers circuit analysis was performed by the HRTEM analysis (Fig. 9(d)). The projection of partial dislocations related to the SF loop can be determined to be 1/12<112>, which would correspond to a 1/6 <112> -type Shockley partial dislocation. The dislocation substructures of the specimen deformed at 870 °C were also examined. Representative TEM micrographs taken along different g vectors are shown in Fig. 10. As the temperature goes above the peak flow temperature, unpaired 1/2<110> dislocations are likely to travel through the {111} planes of the matrix. It either moves toward octahedral {001} planes by cross-slip or dissociates into two super-partials coupled with a SF when encounters the L1$_2$ precipitates, which are highlighted by the green and red circles, respectively. Besides, dislocation dipoles and dislocation bypassing of γ' precipitates were also occasionally observed. Those sessile dislocation substructures would serve

as further barriers for dislocation motions and contribute to sustaining the work hardening at such a high temperature.

4.Discussion

4.1 Effect of alloying elements on the stability of $L1_2$ phase

Phase stability of the $L1_2$ precipitate has long been a critical issue in maintaining desirable mechanical properties for high-temperature materials. Computer-aided calculations of the phase stability, including phase diagram and DFT simulations, have provided valuable information for new alloys development and scientific explanations of some special mechanical behaviors. Yet, most of the previous studies are largely concentrated on the chemically simple intermetallics with constitutions up to three elements. Few of them involve in multicomponent intermetallics that are commonly discovered in the HEA systems, such as the compositionally complex $(Ni, Co, Fe)_3(Ti, Al, Fe)$ [4], $(Ni, Co, Cr)_3(Ti, Al)$ [6], $(Co, Fe, Cr, Ni)_3Ti$ [7] phases, etc.

Here we performed the first-principles calculations to probe the structural stability of the present multicomponent precipitates. Since the Al and Nb elements have a strong tendency to bond with Ni or Co element and form the A_3B structures like the $D0_{22}$, $D0_{19}$ and $L1_2$ phases, these three structures will be considered as competing structures in the present studies. It is worth to note that only a small amount of Fe and Cr could partition into the precipitates according to the APT results (Fig. 6). As a result, for simplification and clarity, supercells containing the major principal elements i.e. $[Ni_{1-x}Co_x]3[Al_{1/2}Nb_{1/2}]$ and $[Ni_{7/24}Co_{7/24}]3[Al_{1-y}Nb_y]$, were applied for the DFT calculations, where x and y range from 0 to 1. The fixed ratios of A site (or B site) for these two configurations are based on the experimentally determined compositions from the

aforementioned APT analysis. Particularly, supercells containing 96, 96 and 64 atoms (192, 192 and 96 atoms) were used to represent the L1$_2$, DO19 and DO$_{22}$ phases of [Ni$_{1-x}$Co$_x$]$_3$[Al$_{1/2}$Nb$_{1/2}$] ([Ni$_{7/24}$Co$_{7/24}$]$_3$[Al$_{1-y}$Nb$_y$]), respectively. The unit cell of each phase was illustrated in Fig. 11(a). First, we evaluated the $\square_f H^0$ values of the [Ni$_{1-x}$Co$_x$]$_3$[Al$_{1/2}$Nb$_{1/2}$] intermetallic compounds with various crystal structures, shown as a function of Co content (Fig. 11(b)). As compared to those of the D0$_{19}$ and D0$_{22}$ structures, the L1$_2$ structure shows a more negative value of $\square_f H^0$ within the whole composition range, demonstrating that the systems with an equal amount of Al and Nb occupied in the B subsites prefer to form L1$_2$ structure. In addition, the $\square_f H^0$ was calculated as a function of Nb substitution of Al from 0 to 1 in the case of [Ni$_{1-x}$Co$_x$]$_3$[Al$_{1/2}$Nb$_{1/2}$], as shown in Fig. 11(c). It can be observed that the L1$_2$ structure is energetically more stable at the range of $0 < y < 0.75$, while the D0$_{19}$ structure will become the prevalent phase when $y > 0.75$. These calculated results are well consistent with our aforementioned experimental observations, where the Al element is a vital ingredient to stabilize the L1$_2$ structure of the (Ni, Co)$_3$Nb-type phase.

4.2 Underlying origins of the deformation mechanisms

Experimental examinations of the deformation substructures (see Figs. 8-10) indicate that the deformation modes of the present L1$_2$- strengthened HEAs are predominantly dominated by the partial dislocations at all temperatures. Specifically, the major deformation mechanisms in the Al4Nb4 HEA consist of the SFs, SF loops coupled with small APBs, SFs together with dislocation cross-slip and bypassing for room temperature, 760 °C and 870 °C, respectively. The yield strength anomaly at 760 °C could thus be attributed to the activation of concurrent slip of paired 1/6<112>

and 1/2<110> super-partial dislocations. More importantly, the sessile nature of these dislocation substructures can further pin the moving dislocations and lead to a sustained work hardening (Fig. 7).

It is also worth noting that such an unusual deformation substructure at 760 °C was seldomly occurred in the tensile-deformed alloys [34-36], which is of great scientific interest and will be carefully discussed in the following section. Enlightened by the scenario in the creep deformed superalloys [36], the formation of isolated SISFs observed here (Fig. 9) may follow the dislocation interaction of 1=2[101]+1/2[011]→1/3[112]+SISF+1/6[112]+APB. In short, the early-formed SISFs will be partially transformed into the APBs by the glide of an ensuing 1/6<112> trailing partial, leaving a loop morphology embedded in the precipitates [37,38]. Basically, to maintain such a dislocation configuration, a critical resolved shear stress t is required to avoid the shrink and annihilation of the loop [37], which could be determined as a function of loop size r:

$$\tau = \frac{\Delta\gamma}{b} - \frac{\mu b}{r} \qquad (2)$$

where $\Delta\gamma = \gamma_{APB} - \gamma_{SISF}$ is the energy difference between the APB and SISF energy, m is the shear modulus of the precipitate, b is the burgers vector of the partial dislocation loop. The flow stress s imposed on the samples during the uniaxial tension could be derived by the equation of $\sigma = M\tau$, where the Taylor factor M≈3.06 is employed for the FCC-type phase [39]. Based on the Eq. (2), a critical gliding force τ_0 is necessarily required to maintain a stable SISF loop with a minimum radius of r0. In other word, when $\tau > \tau_0$, any SISF loops with a radius less than r_0 will shrink and annihilate.

With μ= 90 GPa estimated from the bulk modulus based on the DFT calculations and b = 0.148 nm, the critical flow stress (Fig. 12) as a function of the loop size is plotted in cases of $\Delta\gamma$ equals to 100, 75 and 50 mJ/m², respectively. It can be clearly observed that at the same stress level, the lower bound of the equilibrium size of an isolated SF loop reduces as the energy difference $\Delta\gamma$ increases. As for our present case, the flow stress is approximately 940 MPa at the ~5% true strain (Fig. 7) and the minimum loop radius observed at 760 °C can be determined to be about 8 nm. This means that a critical $\Delta\gamma$ at least over 290 mJ/m² is required. However, such a huge energy difference appears unlikely to be generated in previously reported L1$_2$ phases, as well as the present case. For example, the APB energies of Ni-based L1$_2$ precipitates are typically in the range of 160-295 mJ/m² [40-42], while the SISF energies are around 55-80 mJ/m² based on DFT calculations [43-45]. The difference between them can only reach as large as ~240 mJ/m², suggesting only the loops with a radius larger than ~20 nm can be survived. A similar manner has also been observed in Co-based alloys, where both the APB and SISF energies are generally located within 135-175 mJ/m² [46,47] and the Dg could be even smaller. For the present Al4Nb4 HEA, though the calculations of the SISF energies for the multicomponent L1$_2$ phase is quite complicated, one can roughly estimate the SISF energy on the {111} plane using the axial next-nearest-neighbor Ising model (ANNNI) [48,49]: $\gamma_{SISF} = (E_{D019} - E_{L1_2})/nA$, where E_{D019} and E_{L1_2} are total energies of the L1$_2$ and D0$_{19}$ structures, respectively [46]. A is the area of the fault plane, i.e. the {111} plane here. n is the corresponding number of faulted layers. By this way, the SISF energy on the {111} plane can be estimated to be ~120 mJ/m². Similar to the calculation of SISF energy, the APB energy on {001} planes can be estimated based on the equation of $\gamma_{APB001} = (E_{D0_{22}} - E_{L1_2})/nA$, where $E_{D0_{22}}$ is total energy of the D0$_{22}$ structure, A corresponds to the area of {001} faulted plane. The APB

energy on the {001} plane is thus determined to be ~237 mJ/m^2. Noted that the APBs can only be experimentally observed on the {111} planes in the present Al4Nb4 HEA when deformed at 760 °C. This suggests that the APB energy on the {111} plane of the L1$_2$ phase should be lower than that on the {001} plane, namely 237 mJ/m^2. On the other hand, the Nb atom that generally occupies the Al sublattice is well accepted to increase the APB energy of the Ni3Al (~180 mJ/m^2 [51]). Thus, it is reasonable to believe that the APB energy on the {111} for the L1$_2$ phase in the Al4Nb4 HEA is in the range of 180-237 mJ/m^2. Collectively, the difference between the APB and the SISF energy can be estimated to be 60-117 mJ/m^2, which is much smaller than that of the critically required Dg of 290 mJ/m^2. In other word, the SF loops with a radius of 8 nm could not be retained in this deformed alloy, which is against our experimental observations.

The remaining question arises why the SISF loops can stably exist within the L1$_2$ precipitates. It was argued that the local elemental enrichment near the imperfection would enlarge the energy difference between APB and SISF and consequently promote the formation of SISF loops. In fact, elemental segregations at the SISFs were frequently observed in superalloys. Titus et al. [52] revealed a segregation-assisted diffusive phase transformation (i.e. L1$_2$→D0$_{19}$) in a crept Co-based superalloy and showed the Co/Cr/W enrichment and Ni/Al deficiency at the SISF. Similarly, Smith et al. [53] reported that the faults in the ME501 alloy are enriched with the Nb/Ta/Ti element. The explanations of element diffuse to the faults have been discussed in terms of kinetics and thermodynamics, i.e. (a) elements with the slowest diffusion capacity preferentially segregate to the faults; (b) elements that facilitate to lower the SFE energy tend to segregate to the faults [38]. In the present Al4Nb4 HEA, the Nb atom has the largest atomic radius and highest melting temperature compared to the other constituent elements, which is considered as the slowest diffusion specie and likely to has a higher

tendency to enrich near the faults. The diffusion length required for (a) segregation mechanismis examined and estimated based on the $2\sqrt{Dt}$, where D is the diffusivities of each element, t is the diffusion time. The diffusivities of Ni and Nb were considered here using the diffusivities in a Ni3Al-type intermetallic, which are 1.73×10^{-19} m^2/s and 1.64×10^{-20}m^2/s at 760 °C [54,55], respectively. As a consequence, the Ni atom can diffuse over a distance of ~6 nm within 1 min, while the Nb atom only travels about ~1.9 nm. Such a length scale is large enough to cover the SF region, indicating that the Nb enrichment and Ni depletion at the SF are kinetically possible. That is also consistent with the fact why such a dislocation substructure was more readily initiated in superalloys subjected to high-temperature creep deformation [37,56], where the much longer duration during creep tests enables more pronounced localized heterogeneous elemental distributions. On the other hand, the increase of Nb concentration will dramatically decrease the SISF energy (Fig. 11). For example, the SISF energy will drop from ~120 mJ/m^2 to ~14mJ/m^2 when the Nb concentration increases from 12.5 at.% to 18.5 at.% in the L1$_2$ structure (Fig. 6). The significantly reduced SF energy also drives the segregation process. Yet, experimental efforts on such a segregation behavior remain challenging for us due to the low signal collection efficiency of our TEM. Nevertheless, it is reasonable to conclude that the local elemental segregations driven by lowering SF energy are responsible for the stable formation of SISF loops.

5.Conclusion

In this study, we designed a novel L1$_2$-strengthened (Ni$_2$Co$_2$Fe-Cr)$_{92}$Al$_4$Nb$_4$ high-entropy alloy (HEA), with the Al and Nb elements being the essential L1$_2$ forming elements. This alloy exhibits outstanding tensile strengths that exceed those of most conventional precipitation-hardened HEAs at both room temperature and high

temperatures up to 870 °C, making it an attractive alternative for high-temperature applications. The major conclusions are:

(1) Only the co-addition of Al and Nb elements enables the desired formation of the coherent $L1_2$ precipitates in the Ni-Co-Fe-Cr-Al- Nb HEA system, whereas adding the Al element alone cannot trigger any precipitation reaction and adding the Nb element alone would promote the precipitation of the incoherent $D0_{19}$ phase.

(2) As compared to the Nb4 and Al2Nb4 HEAs, which are either reinforced by $D0_{19}$ phase or the co-precipitated $D0_{19}$ and $L1_2$ phases, the Al4Nb4 HEA primarily strengthened by $L1_2$ precipitates shows an excellent strength-ductility synergy, with a high tensile strength of ~1232 MPa without any ductility loss.

(3) Temperature dependence of the tensile properties was systematically examined, where a flow stress anomaly can be clearly observed at 760 °C. A high yield strength of ~720 MPa can be achieved, which outperforms most of the previous precipitation-hardened HEAs and superalloys due to the relatively large latticemisfit. More importantly, even at the temperature up to 870 °C, a decent strain hardening can bewell retained, leading to a flow stress as high as ~530 MPa.

(4) Shearing of $L1_2$ precipitates by stacking faults was demonstrated as the dominant deformation mode within the temperature ranging from room temperature to 870 °C. Thermally activated dislocation cross-slip and bypassing start to operate in the specimen deformed at 870 °C.

(5) At the anomalous peak temperature of 760 °C, it was proposed that the yield strength anomaly comes from an interesting shearing mode of the $L1_2$ precipitates, in which the shearing occurs predominantly by the passage of super-partial dislocations on the {111} planes, leaving isolated SISF coupled with APB. Such an interesting

deformation substructure could be possibly attributed to the local elemental segregation on the planner faults.

Declaration of Competing Interest

The authors declare that they have no known competing financial interests or personal relationships that could have appeared to influence the work reported in this paper.

Acknowledgment

References

[1] J.W. Yeh, S.K. Chen, S.J. Lin, J.Y. Gan, T.S. Chin, T.T. Shun, C.H. Tsau, S.Y. Chang, Nanostructured high-entropy alloys with multiple principal elements: novel alloy design concepts and outcomes, Adv. Eng. Mater. 6 (2004) 299–303.

[2] D.B. Miracle, O.N. Senkov, A critical review of high entropy alloys and related concepts, Acta Mater. 122 (2017) 448–511.

[3] T. Yang, Y. Zhao, W. Liu, J. Kai, C. Liu, L12-strengthened high-entropy alloys for advanced structural applications, J. Mater. Res. 33 (2018) 2983–2997.

[4] T. Yang, Y.L. Zhao, Y. Tong, Z.B. Jiao, J. Wei, J.X. Cai, X.D. Han, D. Chen, A. Hu, J.J. Kai, K. Lu, Y. Liu, C.T. Liu, Multicomponent intermetallic nanoparticles and superb mechanical behaviors of complex alloys, Science 362 (2018) 933–937.

[5] J.Y. He, H. Wang, Y. Wu, X.J. Liu, H.H. Mao, T.G. Nieh, Z.P. Lu, Precipitation behavior and its effects on tensile properties of FeCoNiCr high-entropy alloys, Intermetallics 79 (2016) 41–52.

[6] Y.L. Zhao, T. Yang, Y. Tong, J. Wang, J.H. Luan, Z.B. Jiao, D. Chen, Y. Yang, A. Hu, C.T. Liu, J.-J. Kai, Heterogeneous precipitation behavior and stacking-fault-mediated deformation in a CoCrni-based medium-entropy alloy, Acta Mater. 138 (2017) 72–82.

[7] Y. Tong, D. Chen, B. Han, J. Wang, R. Feng, T. Yang, C. Zhao, Y.L. Zhao, W. Guo, Y. Shimizu, C.T. Liu, P.K. Liaw, K. Inoue, Y. Nagai, A. Hu, J.J. Kai, Outstanding tensile properties of a precipitation-strengthened FeCoNiCrTi0.2 high-entropy alloy at room and cryogenic temperatures, Acta Mater. 165 (2019) 228–240.

[8] Y.J. Liang, L. Wang, Y. Wen, B. Cheng, Q. Wu, T. Cao, Q. Xiao, Y. Xue, G. Sha, Y. Wang, Y. Ren, X. Li, L. Wang, F. Wang, H. Cai, High-content ductile coherent nanoprecipitates achieve ultrastrong high-entropy alloys, Nat. Commun. 9 (2018) 4063.

[9] N.G. Jones, A. Frezza, H.J. Stone, Phase equilibria of an Al0.5CrFeCoNiCu high entropy alloy, Mater. Sci. Eng. A. 615 (2014) 214–221.

[10] J.Y. He, H. Wang, H.L. Huang, X.D. Xu, M.W. Chen, Y. Wu, X.J. Liu, T.G. Nieh, K. An, Z.P. Lu, A precipitation-hardened high-entropy alloy with outstanding tensile properties, Acta Mater. 102 (2016) 187–196.

[11] A.J. Ardell, Precipitation hardening, Metall. Trans. A. 16 (1985) 2131–2165.

[12] T. Yang, Y.L. Zhao, J.H. Luan, B. Han, J. Wei, J.J. Kai, C.T. Liu, Nanoparticles-strengthened high-entropy alloys for cryogenic applications showing an exceptional strength-ductility synergy, Scr. Mater. 164 (2019) 30–35.

[13] M. Feller-Kniepmeier, T. Link, I. Poschmann, G. Scheunemann-Frerker, C. Schulze, Temperature dependence of deformation mechanisms in a single crystal nickel-base alloy with high volume fraction of γ' phase, Acta Mater. 44 (1996) 2397–2407.

[14] P. Kontis, H.A.M. Yusof, S. Pedrazzini, M. Danaie, K.L. Moore, P.A.J. Bagot, M.P. Moody, C.R.M. Grovenor, R.C. Reed, On the effect of boron on grain boundary character in a new polycrystalline superalloy, Acta Mater. 103 (2016) 688–699.

[15] G. Da Rosa, P. Maugis, A. Portavoce, J. Drillet, N. Valle, E. Lentzen, K. Hoummada, Grain-boundary segregation of boron in high-strength steel studied by nano- SIMS and atom probe tomography, Acta Mater. 182 (2020) 226–234.

[16] R.C. Reed, The superalloys: Fundamentals and Applications, Cambridge University Press, 2008.

[17] D.M. Ceperley, B.J. Alder, Ground state of the electron gas by a stochastic method, Phys. Rev. Lett. 45 (1980) 566–569.

[18] G. Kresse, J. Furthm€uller, Efficient iterative schemes for ab initio total-energy calculations using a plane-wave basis set, Phys. Rev. B - Condens. Matter Mater. Phys. 54 (1996) 11169–11186.

[19] G. Kresse, D. Joubert, From ultrasoft pseudopotentials to the projector augmentedwave method, Phys. Rev. B - Condens. MatterMater. Phys. 59 (1999) 1758–1775.

[20] J.P. Perdew, K. Burke, M. Ernzerhof, Generalized gradient approximation made simple, Phys. Rev. Lett. 77 (1996) 3865–3868.

[21] A. Van De Walle, P. Tiwary, M. De Jong, D.L. Olmsted, M. Asta, A. Dick, D. Shin, Y. Wang, L.Q. Chen, Z.K. Liu, Efficient stochastic generation of special quasirandom structures, Calphad Comput. Coupling Phase Diagr. Thermochem. 42 (2013) 13– 18.

[22] H.J. Monkhorst, J.D. Pack, Special points for Brillouin-zone integrations, Phys. Rev. B. 13 (1976) 5188–5192.

[23] F. Birch, Finite elastic strain of cubic crystals, Phys. Rev. 71 (1947) 809–824.

[24] V. Stevanovic, S. Lany, X. Zhang, A. Zunger, Correcting density functional theory for accurate predictions of compound enthalpies of formation: fitted elementalphase reference energies, Phys. Rev. B - Condens. Matter Mater. Phys. 85 (2012) 115104.

[25] H. Mughrabi, The importance of sign and magnitude of γ/γ' lattice misfit in superalloys - With special reference to the new γ'-hardened cobalt-base superalloys, Acta Mater. 81 (2014) 21–29.

[26] ASM Handbook, Properties and Selection: Irons, Steels and High Performance Alloys, 1, ASM International, 1990.

[27] F. Zhong, S. Li, J. Sha, Tensile behaviour of co-al-w-ta-b-mo alloys with a coherent γ/γ' microstructure at room and high temperatures, Mater. Sci. Eng. A. 637 (2015) 175–182.

[28] H.M. Daoud, A.M. Manzoni, N. Wanderka, U. Glatzel, High-Temperature tensile strength of $Al_{10}Co_{25}Cr_8Fe_{15}Ni_{36}Ti_6$ compositionally complex alloy (High-

Entropy alloy), Jom 67 (2015) 2271–2277.

[29] H.M. Daoud, A. Manzoni, R. Völkl, N. Wanderka, U. Glatzel, Microstructure and tensile behavior of $Al_8Co_{17}Cr_{17}Cu_8Fe_{17}Ni_{33}$ (at.%) high-entropy alloy, JOM 65 (2013) 1805–1814.

[30] J.Y. He, H. Wang, Y. Wu, X.J. Liu, T.G. Nieh, Z.P. Lu, High-temperature plastic flow of a precipitation-hardened FeCoNiCr high entropy alloy, Mater. Sci. Eng. A. 686 (2017) 34–40.

[31] F. Otto, A. Dlouhy, C. Somsen, H. Bei, G. Eggeler, E.P. George, The influences of temperature and microstructure on the tensile properties of a CoCrFeMnNi highentropy alloy, Acta Mater. 61 (2013) 5743–5755.

[32] J. Sato, T. Omori, K. Oikawa, I. Ohnuma, R. Kainuma, K. Ishida, Cobalt-base hightemperature alloys, Science 312 (2006) 90–91.

[33] D.B. Williams, C.B. Carter, Transmission Electron Microscopy: A Textbook For Materials Science, Springer, 2009.

[34] Y.Q. Sun, P.M. Hazzledine, A tem weak-beam study of dislocations in g' in a deformed Ni-based superalloy, Philos. Mag. A Phys. Condens. Matter Struct. Defects Mech. Prop. 58 (1988) 603–617.

[35] A. Suzuki, G.C. DeNolf, T.M. Pollock, Flow stress anomalies in γ/γ' two-phase Co- Al-W-base alloys, Scr. Mater. 56 (2007) 385–388.

[36] A. Suzuki, T.M. Pollock, High-temperature strength and deformation of γ/γ' twophase Co-Al-W-base alloys, Acta Mater. 56 (2008) 1288–1297.

[37] Y.M. Eggeler, J. M€uller, M.S. Titus, A. Suzuki, T.M. Pollock, E. Spiecker, Planar defect formation in the γ' phase during high temperature creep in single crystal

CoNibase superalloys, Acta Mater 113 (2016) 335–349.

[38] S.K. Makineni, A. Kumar, M. Lenz, P. Kontis, T. Meiners, C. Zenk, S. Zaefferer, G. Eggeler, S. Neumeier, E. Spiecker, D. Raabe, B. Gault, On the diffusive phase transformation mechanism assisted by extended dislocations during creep of a single crystal CoNi-based superalloy, Acta Mater. 155 (2018) 362–371.

[39] J.F.W. Bishop, R. Hill, A theory of the plastic distortion of a polycrystalline aggregate under combined stresses, Lond. Edinb. Dublin Philos. Mag. J. Sci. 42 (1951) 414–427.

[40] H.P. Karnthaler, E.T. Mühlbacher, C. Rentenberger, The influence of the fault energies on the anomalous mechanical behaviour of Ni_3Al alloys, Acta Mater. 44 (1996) 547–560.

[41] D.M. Dimiduk, A.W. Thompson, J.C. Williams, The compositional dependence of antiphase-boundary energies and the mechanism of anomalous flow in Ni_3Al alloys, Philos. Mag. A Phys. Condens. Matter Struct. Defects Mech. Prop. 67 (1993) 675–698.

[42] T. Kruml, E. Conforto, B. Lo Piccolo, D. Caillard, J.L. Martin, From dislocation cores to strength and work-hardening: a study of binary Ni_3Al, Acta Mater. 50 (2002) 5091–5101.

[43] A. Breidi, J. Allen, A. Mottura, First-principles modeling of superlattice intrinsic stacking fault energies in Ni_3Al based alloys, Acta Mater. 145 (2018) 97–108.

[44] O.N. Mryasov, Y.N. Gornostyrev, M. Van Schilfgaarde, A.J. Freeman, Superdislocation core structure in L12 Ni_3Al, Ni3Ge and Fe_3Ge: Peierls-Nabarro analysis starting from ab-initio GSF energetics calculations, Acta Mater. 50 (2002)

4545–4554.

[45] G. Schoeck, S. Kohlhammer, M. Fahnle, Planar dissociations and recombination energy of [110]superdislocations in Ni$_3$Al: generalized Peierls model in combination with ab initio electron theory, Philos. Mag. Lett. 79 (1999) 849–857.

[46] A. Mottura, A. Janotti, T.M. Pollock, A first-principles study of the effect of Ta on the superlattice intrinsic stacking fault energy of L12-Co3(Al,W), Intermetallics 28 (2012) 138–143.

[47] N.L. Okamoto, T. Oohashi, H. Adachi, K. Kishida, H. Inui, P. Veyssiere, Plastic deformation of polycrystals of Co$_3$(Al,W) with the L1$_2$ structure, Philos. Mag. 91 (2011) 3667–3684.

[48] P.J.H. Denteneer, J.M. Soler, Energetics of point and planar defects in aluminium from first-principles calculations, Solid State Commun. 78 (1991) 857–861.

[49] P.J.H. Denteneer, W. Van Haeringen, Stacking-fault energies in semiconductors from first-principles calculations, J. Phys. C Solid State Phys. 20 (1987) L883–L887.

[50] C. Colinet, A. Pasturel, Structural stability of one-dimensional long-period structures in the TiAl$_3$ compound, J. Phys. Condens. Matter. 14 (2002) 6713–6727.

[51] N.M. Rosengaard, H.L. Skriver, Ab initio study of antiphase boundaries and stacking faults in L1$_2$ and D0$_{22}$ compounds, Phys. Rev. B. 50 (1994) 4848–4858.

[52] M.S. Titus, A. Mottura, G. Babu Viswanathan, A. Suzuki, M.J. Mills, T.M. Pollock, High resolution energy dispersive spectroscopy mapping of planar defects in L1$_2$- containing Co-base superalloys, Acta Mater. 89 (2015) 423–437.

[53] T.M. Smith, B.D. Esser, N. Antolin, A. Carlsson, R.E.A. Williams, A.

Wessman, T. Hanlon, H.L. Fraser, W. Windl, D.W. McComb, M.J. Mills, Phase transformation strengthening of high-temperature superalloys, Nat. Commun. 7 (2016) 1–7.

[54] K. Fujiwara, Z. Horita, Measurement of intrinsic diffusion coefficients of Al and Ni in Ni_3Al using Ni/NiAl diffusion couples, Acta Mater. 50 (2002) 1571–1579.

[55] J. Cermak, A. Gazda, V. Rothova, Interdiffusion in ternary Ni_3Al/Ni_3Al-X diffusion couples with x = Cr, Fe, Nb and Ti, Intermetallics 11 (2003) 939–946.

[56] G.B. Viswanathan, P.M. Sarosi, M.F. Henry, D.D. Whitis, W.W. Milligan, M.J. Mills, Investigation of creep deformation mechanisms at intermediate temperatures in Rene 88 DT, Acta Mater. 53 (2005) 3041–3057.
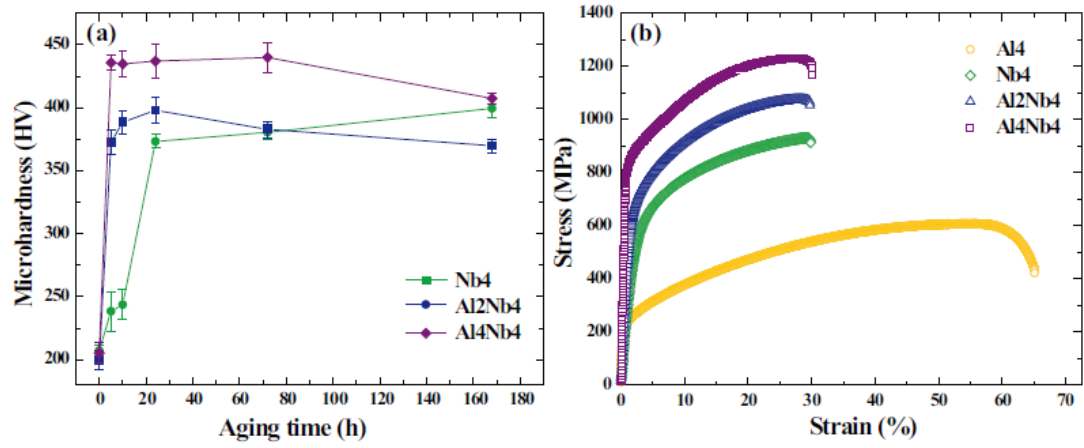
Fig. 1. (a) Microhardness evolutions of the Nb4, Al2Nb4 and Al4Nb4 HEAs as a function of the aging time. (b) Representative room-temperature tensile stress-strain curves of the HEAs aged at 800 °C for 24 h.
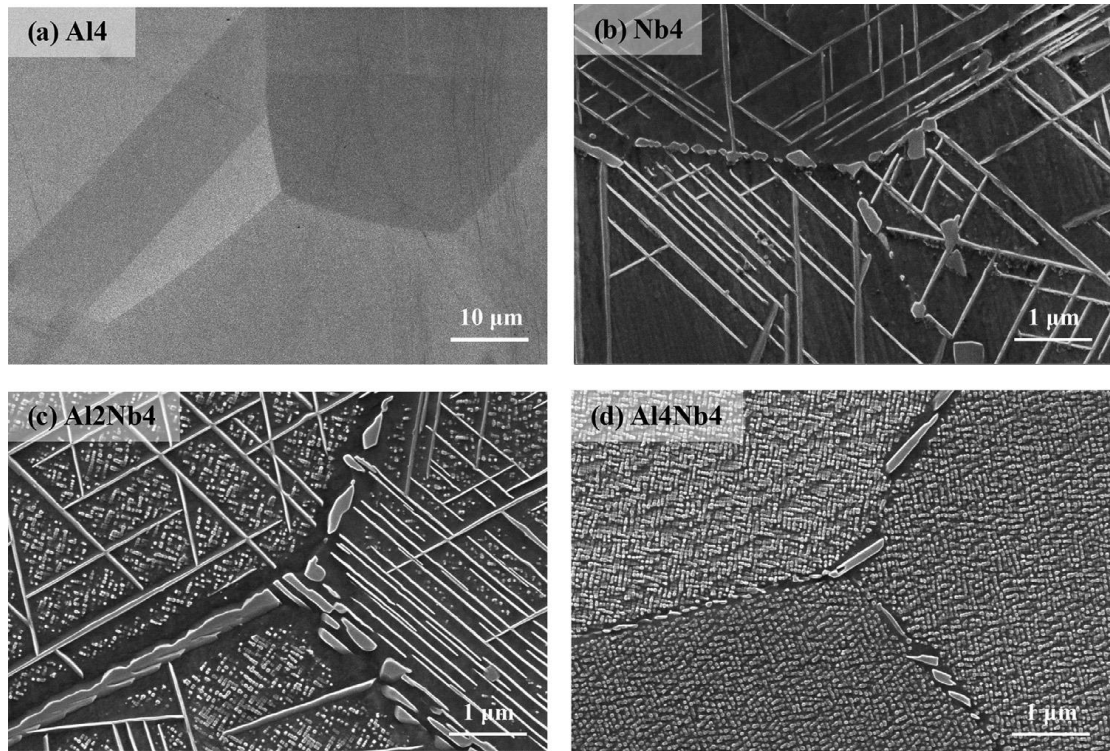
Fig. 2. SEM images showing the typical microstructures of the Al4, Nb4, Al2Nb4 and Al4Nb4 HEAs aged at 800 °C for 24 h.
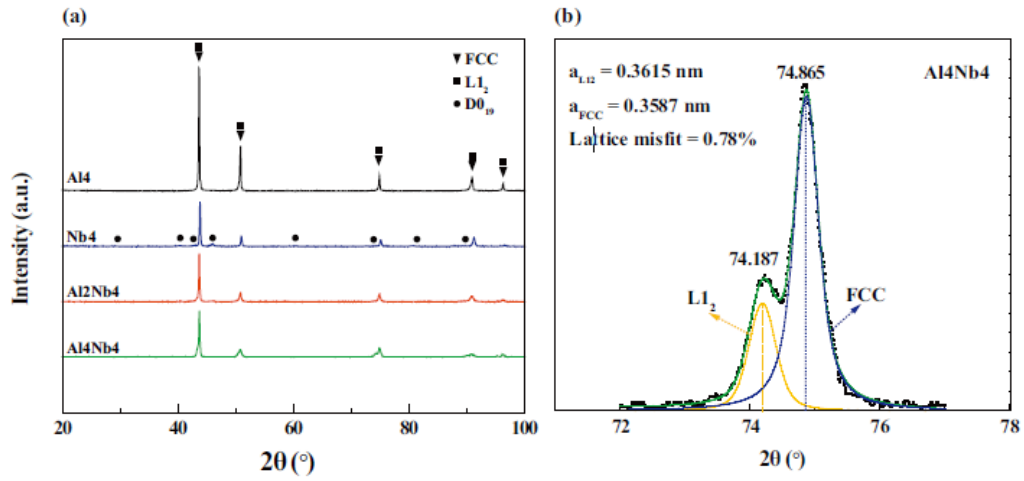
Fig. 3. (a) XRD patterns of the HEAs after 24 h aging at 800 °C. (b) Deconvolution of the (220) diffraction peak of the Al4Nb4 alloy showing the lattice misfit between the particles and matrix.
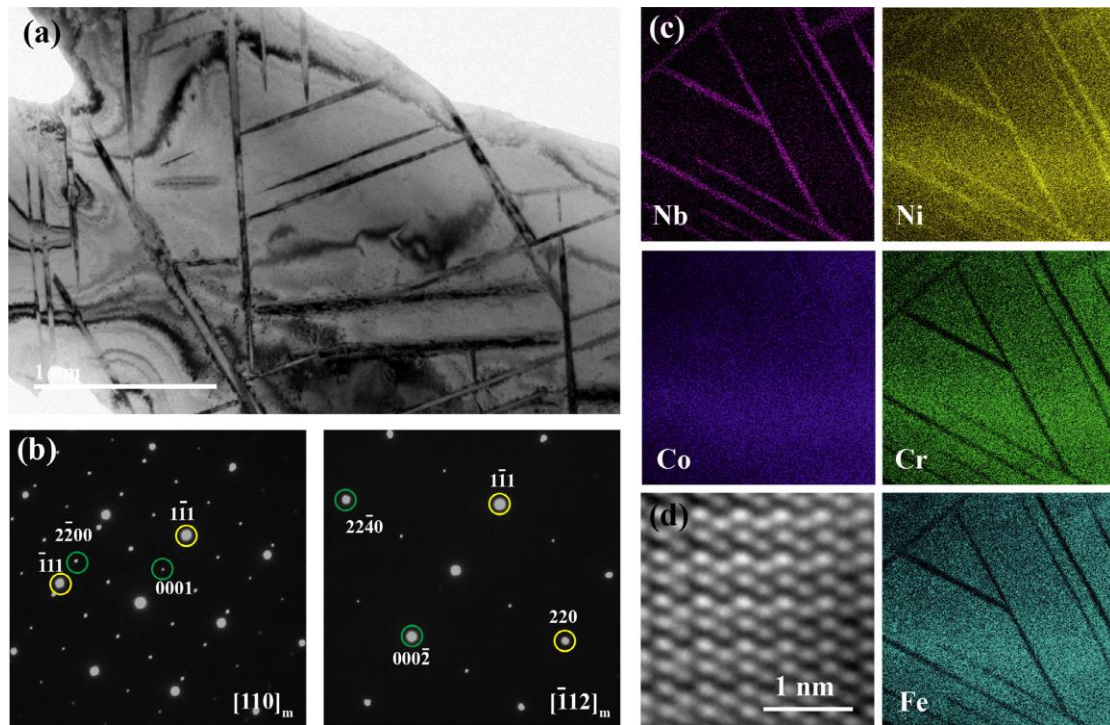
Fig. 4. (a) Bright-field image showing the needle-shaped precipitates in the Nb4 HEA and (b) low-index diffraction patterns taken along $[110]_m$ and $[112]_m$ zone axes of the matrix. (c) EDS compositional maps showing the elemental distributions of each element labeled in the figures. (d) HRTEM image of the needle-shaped precipitates.
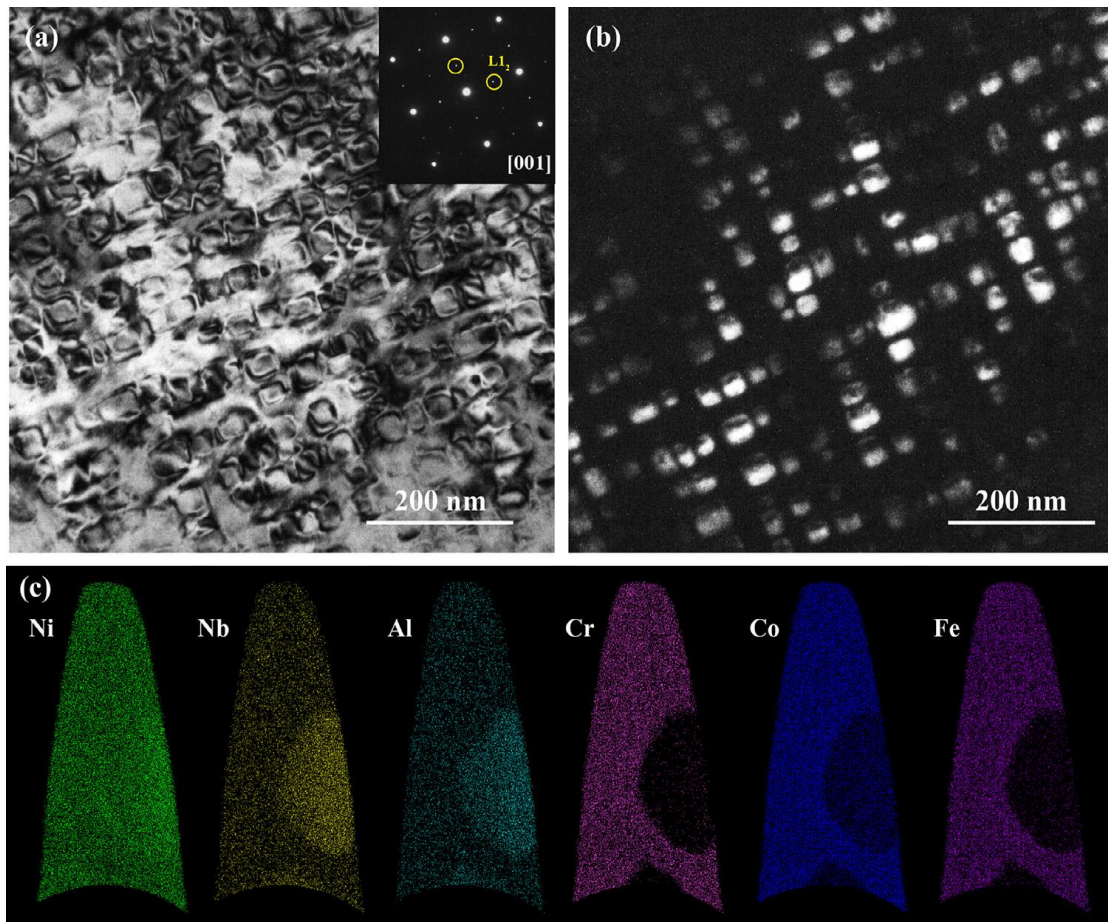
Fig. 5. (a) Typical bright-field micrograph showing the microstructure of the Al4Nb4 HEA. (b) Dark-field micrograph obtained from the superlattice spot corresponding to the ordered structure. (c) Ion maps of the individual elements.
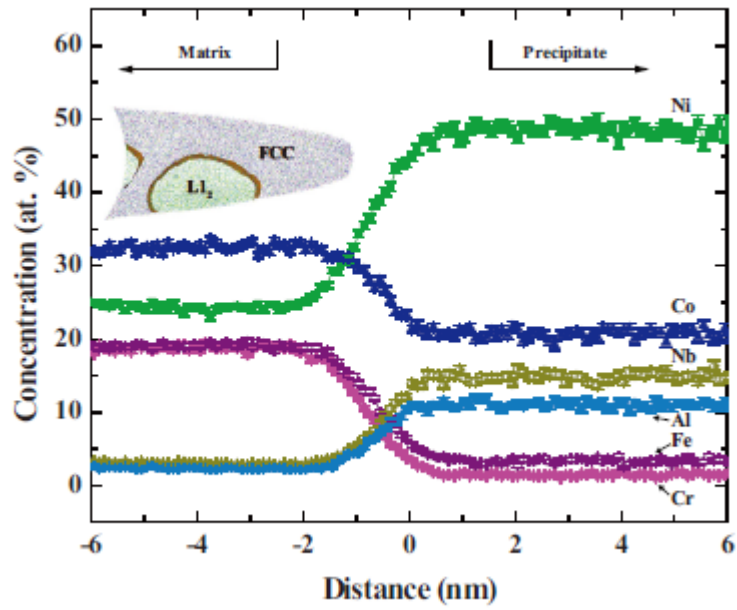
Fig. 6. Proximity histogram across the matrix/precipitate interface. The interface was highlighted by the 10 at.% Nb iso-concentration surface in a reconstructed slice of the APT tip, shown as the inset.
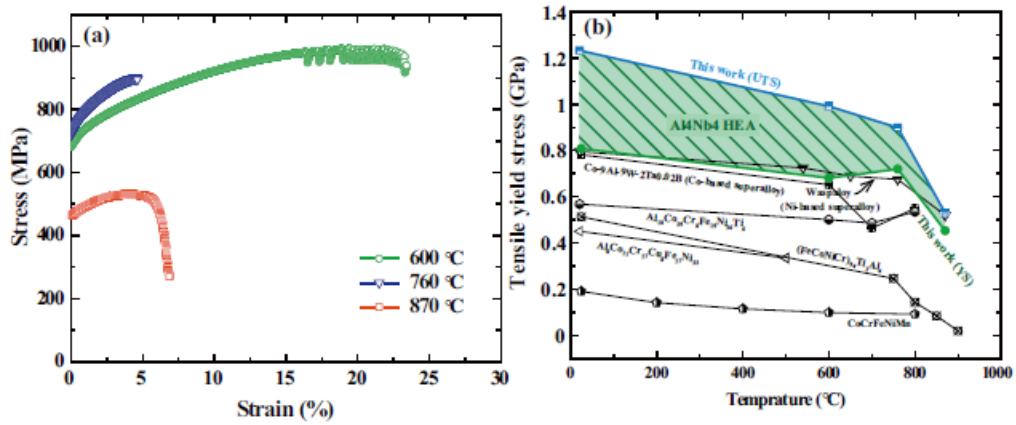
Fig. 7. (a) High-temperature stress-strain curves of the Al4Nb4 HEA subjected to tensile strain. (b) Comparison of the YS and UTS as a function of temperature with the tensile YS of the Waspaloy (Ni-based superalloy) [26], Co-Al-W-Ta-B (Co-based superalloy) [27] and other HEAs [28-31].
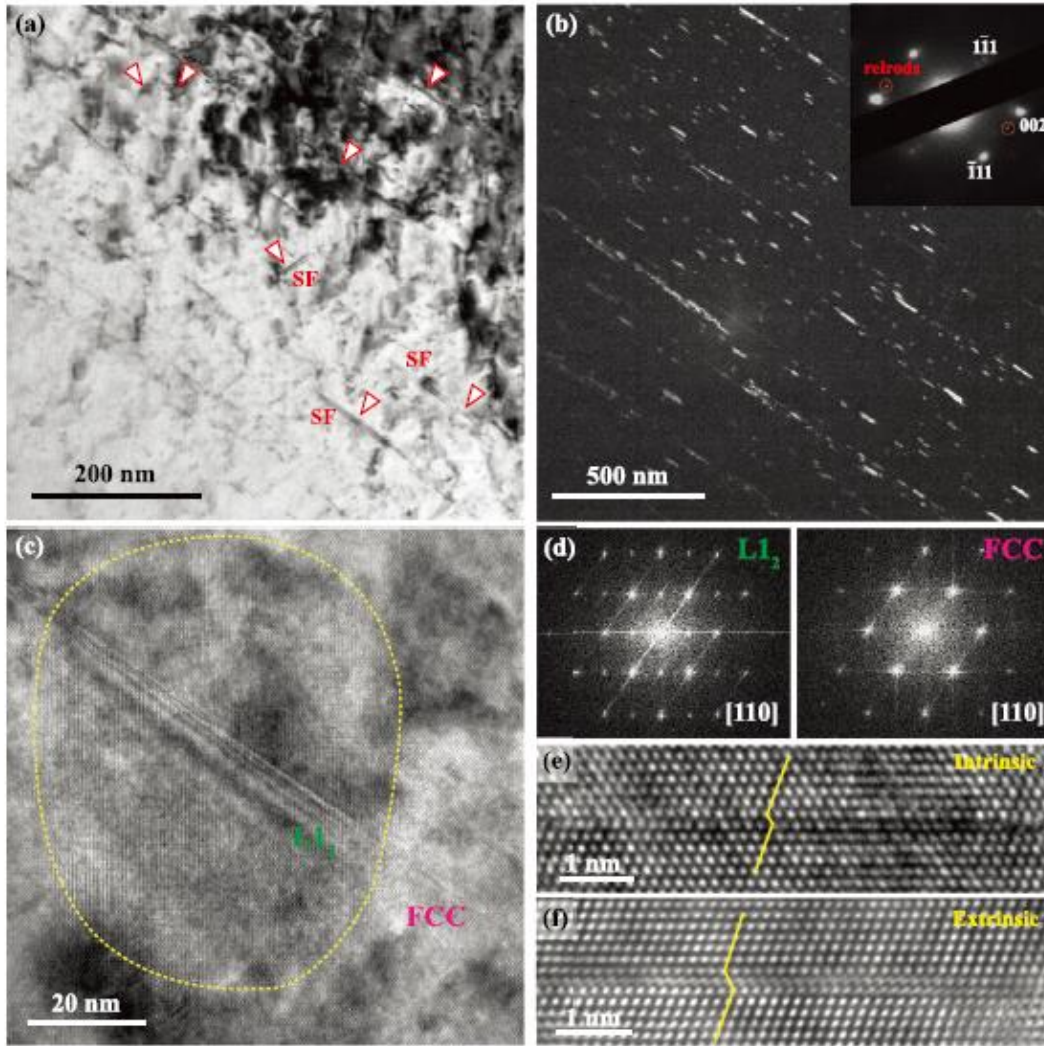
Fig. 8. (a) Deformation substructures of the Al4Nb4 HEA deformed at room temperature. (b) Dark-field TEM image taken from the relrods of the SFs. (c) HRTEM image gives a typical example of the L12 precipitate sheared by the SFs. The corresponding FFT images for the L12 precipitates and the matrix in (c) are shown in (d). (e) and (f) illustrate the characteristics of the SFs found in the deformed sample.
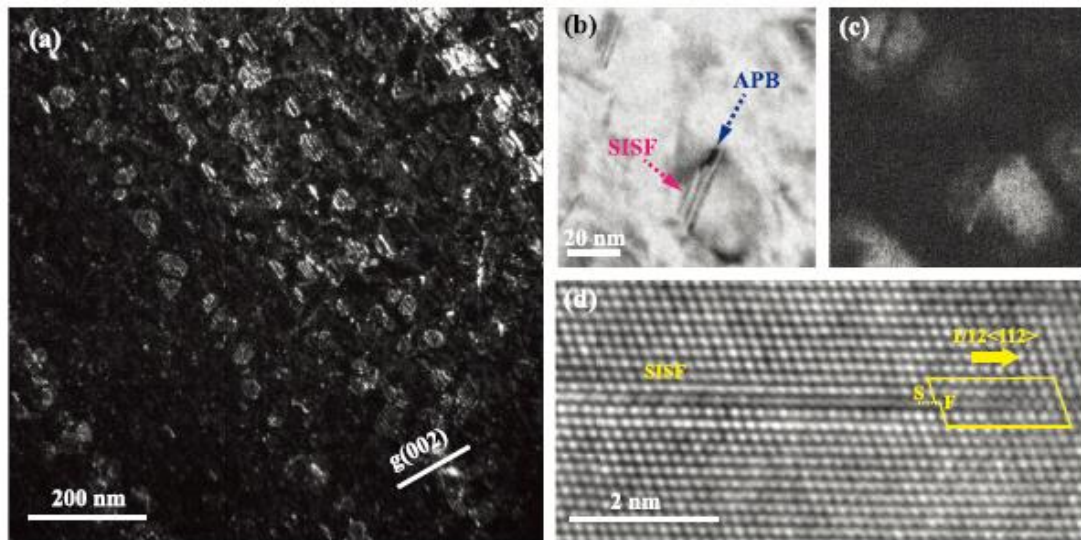
Fig. 9. (a) Typical dislocation substructures in the Al4Nb4 HEA deformed at the peak flow temperature of 760 °C, showing the superlattice SF loops embedded within the L1$_2$ precipitates. (b) Bright-field and (c) dark-field TEM micrographs clearly showing the SISF/APB defect configuration in the L12 precipitates. The Burgers vector of those SF loops are determined to be 1/6<112> type in (d).
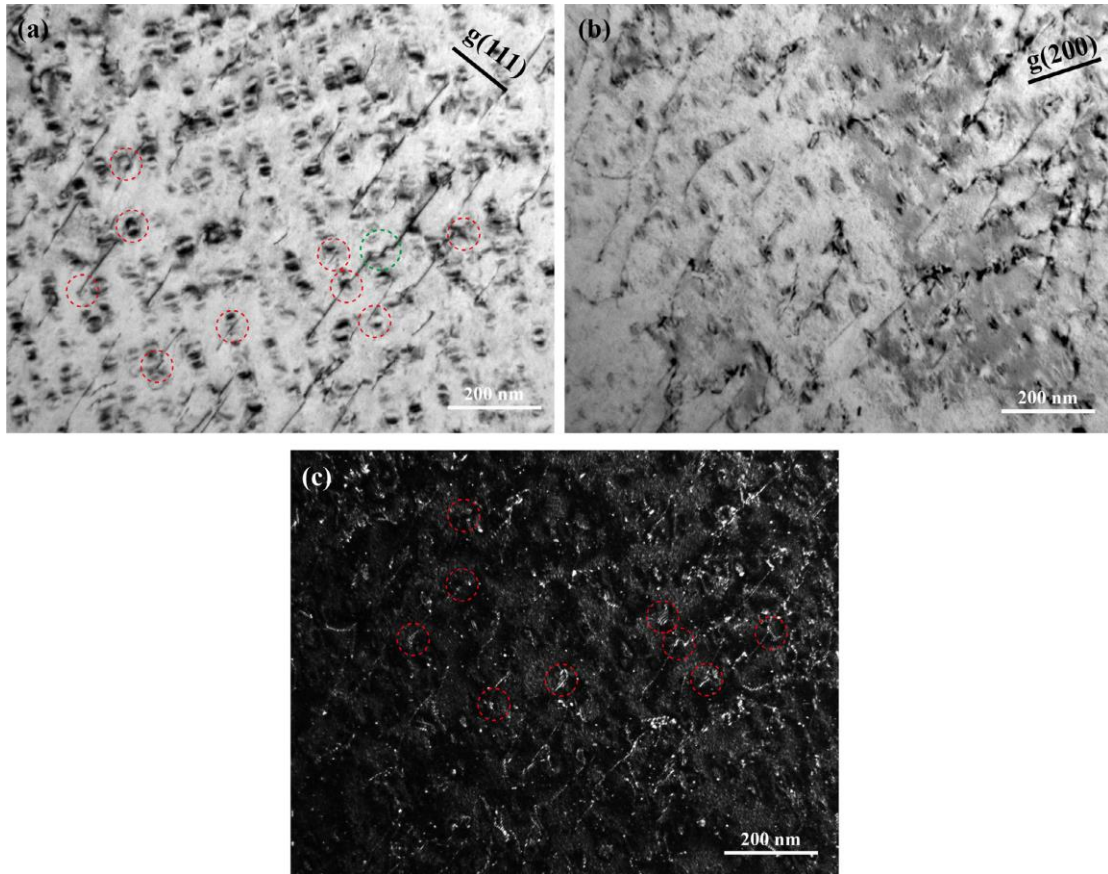
Fig. 10. Series of TEM bright-field and dark-field images of the Al4Nb4 HEA deformed at 870 °C (a) B = [011], g = (111); (b) B =[001], g = (200); (c) is the near g/4 g weak beam darkfield of (b), where B is the nearest zone axis. Dislocation dissociation and cross-slip are highlighted by the red and green circle, respectively. (For interpretation of the references to color in this figure legend, the reader is referred to the web version of this article.)
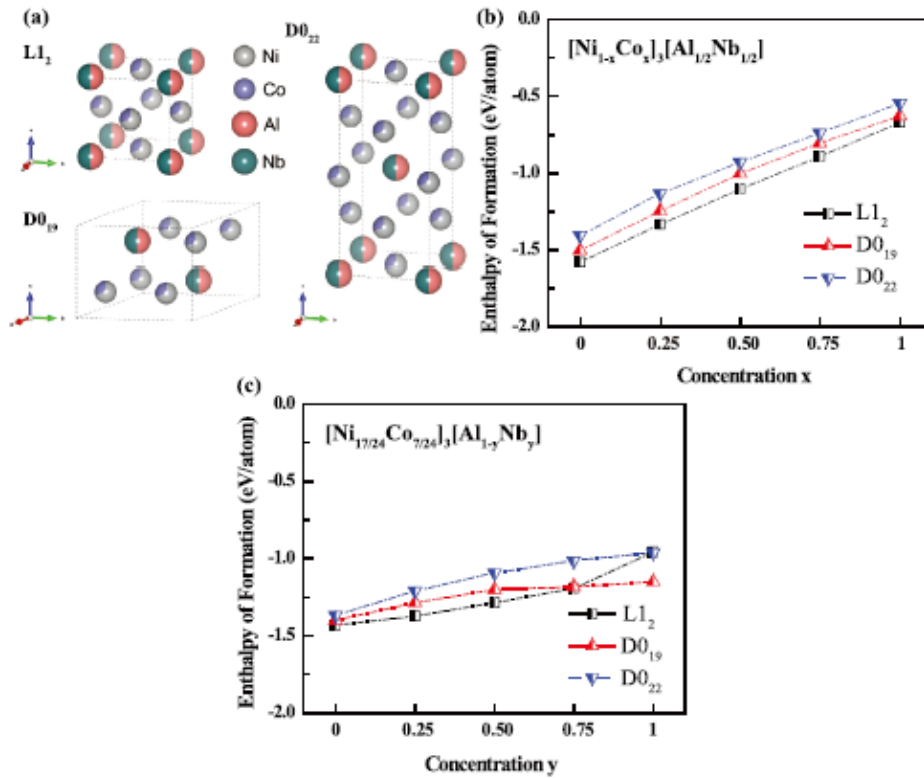
Fig. 11. (a) Crystal structures of the L12, D019 and D022 phases. Calculated formation enthalpies of each phase in (c) $Ni_{1-x}Co_x]_3[Al_{1/2}Nb_{1/2}]$ and (d) $[Ni_{7/24}Co_{7/24}]_3[Al_{1-y}Nb_y]$, where x and y range from 0 to 1.
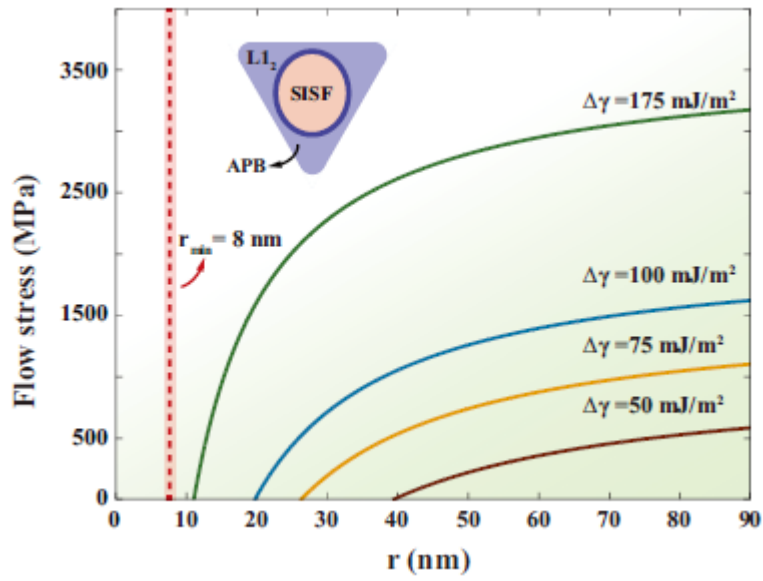
Fig. 12. The critical stress required for the stabilization of the SF loop with a radius of r formed within the L1$_2$ precipitate.